entropy

IMPACT FACTOR 2.1

Indexed in: PubMed

CITESCORE 4.9

Article

Survival Probability, Particle Imbalance, and Their Relationship in Quadratic Models

Miroslav Hopjan and Lev Vidmar

MDPI

https://doi.org/10.3390/e26080656

entropy

MDPI

Article

Survival Probability, Particle Imbalance, and Their Relationship in Quadratic Models

Miroslav Hopjan [1,*] **and Lev Vidmar** [1,2]

[1] Department of Theoretical Physics, J. Stefan Institute, SI-1000 Ljubljana, Slovenia; lev.vidmar@ijs.si
[2] Department of Physics, Faculty of Mathematics and Physics, University of Ljubljana, SI-1000 Ljubljana, Slovenia
* Correspondence: miroslav.hopjan@ijs.si

Abstract: We argue that the dynamics of particle imbalance in quadratic fermionic models is, for the majority of initial many-body product states in the site occupation basis, virtually indistinguishable from the dynamics of survival probabilities of single-particle states. We then generalize our statement to a similar relationship between the non-equal time and space density correlation functions in many-body states, and the transition probabilities of single-particle states at nonzero distances. Finally, we study the equal-time connected density–density correlation functions in many-body states, which exhibit certain qualitative analogies with the survival and transition probabilities of single-particle states. Our results are numerically tested for two paradigmatic models of single-particle localization: the 3D Anderson model and the 1D Aubry–André model. This work gives an affirmative answer to the question of whether it is possible to measure features of single-particle survival and transition probabilities by the dynamics of observables in many-body states.

Keywords: survival probability; particle imbalance; quantum quench dynamics; quadratic fermionic models; eigenstate transitions

Citation: Hopjan, M.; Vidmar, L. Survival Probability, Particle Imbalance, and Their Relationship in Quadratic Models. *Entropy* **2024**, *26*, 656. https://doi.org/10.3390/e26080656

Academic Editor: Giuliano Benenti

Received: 3 June 2024
Revised: 28 July 2024
Accepted: 29 July 2024
Published: 31 July 2024

1. Introduction

The survival probability of an initial state $|j\rangle$ is defined as the square of its overlap with the time-evolving quantum state $|j(t)\rangle = e^{-i\hat{H}t}|j\rangle$ under the Hamiltonian $\hat{H}$,

$$P_{jj}^{H}(t) = |\langle j|e^{-i\hat{H}t}|j\rangle|^2 \,, \tag{1}$$

where we set $\hbar = 1$. It represents a useful probe to study the dynamical properties of $\hat{H}$ and, hence, it is of broad interest in the theory of quantum chaos and ergodicity breaking phenomena [1–22]. For example, it was shown that the averaged survival probability,

$$P^{H}(t) = \langle P_{jj}^{H}(t) \rangle_j \,, \tag{2}$$

represents a particularly useful tool for the detection of eigenstate transitions [20,21]. The average $\langle \ldots \rangle_j$ in Equation (2) is carried out over all possible initial states $|j\rangle$ that can be thought of as the eigenstates of the Hamiltonian $\hat{H}_0$ before the quench. The eigenstate transitions may correspond to single-particle localization transitions in eigenstates of $\hat{H}$ when the initial states $|j\rangle$ are single-particle states, or ergodicity breaking phase transitions when the initial states $|j\rangle$ are many-body states.

Here, we study quadratic fermionic models and search for quantitative similarities between the dynamics of single-particle quantities, such as survival probability and the dynamics of observables in many-body states. Recently, we reported the observation that the dynamics of site occupations and particle imbalance (to be defined below) exhibit critical behavior at the localization transition point [23], similar to the critical behavior of

survival probability [20,21]. This observation corresponds to the dynamics of the initial many-body states that are charge density-wave (CDW) product states at half filling, i.e., the states that are routinely studied in experiments [24–30]. The property of the CDW product states is that the neighboring sites of an occupied lattice site are always empty, at least along a selected direction. The particle imbalance is defined as the normalized sum of weighted site occupations $n_j^H(t)$ over the entire lattice with V sites,

$$I^H(t) = \frac{2}{V}\sum_{j=1}^{V}(-1)^{n_j(0)-1} n_j^H(t)\,, \quad \text{with} \quad n_j^H(t) = \langle\Psi_0|e^{i\hat{H}t}\hat{n}_j e^{-i\hat{H}t}|\Psi_0\rangle\,, \tag{3}$$

where $\hat{n}_j = \hat{c}_j^\dagger \hat{c}_j$ is the site-occupation (density) operator, $|\Psi_0\rangle$ is the initial many-body state, $n_j(0)$ is the site occupation at time $t = 0$, and the prefactor $2/V$ assures the unit normalization at $t = 0$. The imbalance can also be expressed as the mean of the site-occupation (density) autocorrelation functions,

$$I^H(t) = \frac{4}{V}\sum_{j=1}^{V}\Big[n_j^H(t) - 1/2\Big]\Big[n_j(0) - 1/2\Big]\,. \tag{4}$$

The property that one may detect the eigenstate transitions via the dynamics of particle imbalance [23] shares similarities with the detection of eigenstate transitions via the survival probability [20,21]. Intriguingly, even the exponent β_I of the power-law decay of imbalance at criticality from the initial CDW product states is quantitatively close to the decay exponent β of the survival probability in the 3D Anderson model, though it is dissimilar in the 1D Aubry–André model. Similarities between the density-wave imbalance and the survival probability were also studied in delocalized disordered systems [31]. These results call for a more detailed understanding of the connection of the dynamics of density correlations in many-body states with the dynamics of single-particle quantities such as survival probabilities.

In this work, we go beyond Ref. [23] and focus on the quantitative comparison between the dynamics in many-body states and single-particle states, ranging from short to long times, considering initial many-body product states on a site occupation basis without the CDW order, as well as tuning the disorder strength to the localization transition point and away from it. Our study is carried out while having in mind the 3D Anderson model and 1D Aubry–André model (to be introduced in Section 2); however, we expect our results to generally apply to quadratic models with quenched disorder and localization transitions. The main result of this work is that for the overwhelming majority of initial many-body product states on a site occupation basis, dubbed typical product states, the dynamics of particle imbalance are virtually indistinguishable from the dynamics of single-particle survival probabilities,

$$I^H(t) \approx P^H(t)\,. \tag{5}$$

The derivation of Equation (5) and its numerical tests are carried out in Section 3. In Section 4, we generalize this result to a similar relationship between the non-equal time and space density correlation functions and the single-particle transition probabilities between lattice sites at non-zero distances. In Section 5, we discuss qualitative similarities between the dynamics of equal-time connected density–density correlation functions and the dynamics of single-particle survival and transition probabilities. We conclude in Section 6.

2. Models

We consider two paradigmatic quadratic models of fermions without spin structure that exhibit single-particle localization transitions, the Anderson model [32–34] and the Aubry–André model [35,36]. The models are given by the Hamiltonian

$$\hat{H} = -J \sum_{\langle ij \rangle} (\hat{c}_i^\dagger \hat{c}_j + \hat{c}_j^\dagger \hat{c}_i) + \sum_{i=1}^{V} \epsilon_i \hat{n}_i \,, \tag{6}$$

where $\langle ij \rangle$ denotes nearest neighbors, J stands for the strength of hopping matrix element linking the nearest neighbors, $\hat{c}_i^\dagger$ ($\hat{c}_i$) are the fermionic creation (annihilation) operators at site i, $\hat{n}_i = \hat{c}_i^\dagger \hat{c}_i$ is the site occupation (density) operator, and ϵ_i represents the on-site energy. The number of lattice sites is denoted as V, which also equals the single-particle Hilbert space dimension D, i.e., $D = V$.

As the first example, we inspect the Anderson model on a three-dimensional (3D) cubic lattice of volume $V = L^3$, where L is the linear size, with periodic boundary conditions. The on-site energies ϵ_i are independently and identically distributed, their values are taken out from a box distribution $\epsilon_i \in [-W/2, W/2]$. Properties of the 3D Anderson model have been discussed in several reviews [34,37–40]; below, we summarize some of them that are relevant for this study. The position of the localization critical point and its properties were discussed from different perspectives [37,40–43], with the broad acceptance that the system is insulating—i.e., with all single-particle eigenstates localized—for $W > W_c \approx 16.5\,J$ [44]. For $W < W_c$, the transport is dominated by diffusive eigenstates [7,45,46]. At the critical point, the diffusive eigenstates vanish and the multifractal eigenstates [34,47,48] govern the transport that then becomes subdiffusive [7]. Moreover, below the critical disorder $W < W_c$, mobility edges in the spectrum separate the localized eigenstates from the delocalized ones. The mobility edges shift towards the band edges when disorder is decreased [49]. Whereas the localization transition is typically studied within the framework of single-particle properties, its manifestations can also be detected in many-body states [23,45,50–52].

The second model that we inspect is the Aubry–André model on a one-dimensional (1D) lattice of size L with closed boundary conditions. In this model, the quasiperiodic on-site potential $\epsilon_i = \lambda \cos(2\pi q i + \phi)$ is imposed on the lattice, λ represents the amplitude of the potential, and ϕ is a global phase. The periodicity of the potential is incommensurate with the periodicity of the lattice by the standard choice of the golden ratio value $q = \frac{\sqrt{5}-1}{2}$. Its properties were discussed in Ref. [53], and below we limit the discussion to those that are relevant for this study. At $\lambda_c = 2J$, the 1D Aubry–André model displays an abrupt transition from delocalized to localized phase [35,36,50,54–61]. The model shows self-dual property. On the one hand, at $\lambda > \lambda_c$, all states are localized in real space with delocalization exhibited in momentum space; on the other hand, at $\lambda < \lambda_c$, all states are delocalized in real space with localization exhibited in momentum space. At $\lambda = \lambda_c$, i.e., the critical point, both the eigenspectrum and eigenstates are (multi)fractal, and the model exhibits diffusion [62] or atypical scaling $\propto L^2$ of the typical Heisenberg time [20]. The latter can be understood as a remnant two-dimensionality of the 1D Aubry–André model. Indeed, the model is closely associated to the Harper–Hofstadter model, which describes an electron moving in an isotropic 2D lattice subjected to magnetic field [63]. The transition was experimentally realized using photonic lattices [64] and cold atoms [65,66]. As in the Anderson model, the localization transition in the 1D Aubry–André model is typically studied within the framework of single-particle properties; however, its manifestations can also be detected in many-body states [23,50,51,67–70].

3. Survival Probability and Particle Imbalance

We consider the following quench protocol. The initial Hamiltonian is $\hat{H}_0 = \sum_{i=1}^{V} \epsilon_i \hat{n}_i$, which can be thought of as the limit of infinite-strength disorder, and the final Hamiltonian $\hat{H}$ is given by Equation (6). The initial many-body states $|\Psi_0\rangle$ are eigenstates of $\hat{H}_0$ and can be written as product states on a site occupation basis,

$$|\Psi_0\rangle = \prod_{j_l \in \Psi_0} \hat{c}_{j_l}^\dagger |\varnothing\rangle \,, \tag{7}$$

where the product runs over the sites j_l that are occupied in the initial states (we consider half filling, i.e., the number of particles is $N = V/2$). The time evolution of the particle occupation n_j^H at site j can be expressed as [23]

$$n_j^H(t) = \sum_{j_l \in \Psi_0} P_{jj_l}^H(t) \,, \tag{8}$$

where we introduce the time evolution of single-particle transition probabilities

$$P_{jj_l}^H(t) = |\langle j|e^{-i\hat{H}t}|j_l\rangle|^2 \,, \tag{9}$$

from the initially occupied single-particle state $|j_l\rangle$ to the state $|j\rangle$. We stress that the simple relation in Equation (8) between the time evolution of observable in many-body states and the transition probabilities of single-particle states applies only for the observables that share the common eigenbasis with the Hamiltonian $\hat{H}_0$ before the quench—see the detailed derivation in Ref. [23].

Equation (8) allows one to explicitly connect the dynamics of site occupations in many-body states with the single-particle survival probability. For the initially occupied sites, $_{j\in\Psi_0}$, the contribution of the single-particle survival probability can be taken out of the sum in Equation (8),

$$n_{j\in\Psi_0}^H(t) = P_{jj}^H(t) + \sum_{j_l \in \Psi_0}^{j_l \neq j} P_{jj_l}^H(t) \,. \tag{10}$$

The time evolution of the particle imbalance $I^H(t)$ in Equation (3) can then be expressed only via the site occupations of the initially occupied sites,

$$I^H(t) = \frac{2}{V}\sum_{j\in\Psi_0} n_j^H(t) - \frac{2}{V}\sum_{j\notin\Psi_0} n_j^H(t) = \langle n_j^H(t)\rangle_{j\in\Psi_0} - \langle n_j^H(t)\rangle_{j\notin\Psi_0} = 2\langle n_j^H(t)\rangle_{j\in\Psi_0} - 1 \,, \tag{11}$$

where we define the average over initially occupied sites $\langle \dots \rangle_{j\in\Psi_0} = \frac{2}{V}\sum_{j\in\Psi_0}\dots$ (with $j \in \Psi_0 \to j \notin \Psi_0$ for the average over initially unoccupied sites) and we used the particle sum rule $\langle n_j^H(t)\rangle_{j\in\Psi_0} + \langle n_j^H(t)\rangle_{j\notin\Psi_0} = 1$.

Equation (11) provides the basis for our derivation of Equation (5). To this end, we substitute Equation (10) into Equation (11) and separate the contribution from the survival probabilities as

$$I^H(t) = \langle\, P_{jj}^H(t)\,\rangle_{j\in\Psi_0} + \left\langle P_{jj}^H(t) + 2\sum_{j_l\in\Psi_0}^{j_l\neq j} P_{jj_l}^H(t)\right\rangle_{j\in\Psi_0} - 1 \,. \tag{12}$$

This equation suggests that the particle imbalance and survival probability become identical if the second and the third term on the r.h.s. of Equation (12) cancel, i.e., if

$$\left\langle P_{jj}^H(t) + 2\sum_{j_l\in\Psi_0}^{j_l\neq j} P_{jj_l}^H(t)\right\rangle_{j\in\Psi_0} = 1 \,. \tag{13}$$

However, this is in general not the case and, hence, the formal equivalence between the particle imbalance and survival probabilities is not expected to hold.

At this point, one can ask whether there exist initial states for which the particle imbalance and survival probabilities still become approximately identical. We argue that this is indeed the case for the overwhelming majority of initial many-body states under consideration. We refer to them as typical initial product states. At half filling, the sites j of a typical initial product state have their neighbors occupied or not occupied with equal

probability. This gives rise to the self-averaging property of the wavefunction, since the sum on the l.h.s. of Equation (13) can be expressed as

$$\left\langle P_{jj}^{H}(t) + 2\sum_{j_l\in\Psi_0}^{j_l\neq j} P_{jj_l}^{H}(t) \right\rangle_{j\in\Psi_0} \approx \left\langle P_{jj}^{H}(t) + \frac{2}{2}\sum_{\substack{i=1\\ i\neq j}}^{V} P_{ji}^{H}(t) \right\rangle_{j\in\Psi_0} = \left\langle \sum_{i} P_{ji}^{H}(t) \right\rangle_{j\in\Psi_0} = 1\,, \quad (14)$$

where in the last step we have used the conservation of all transition probabilities, including the survival probability $\sum_i P_{ji}^{H}(t) = 1$. Thus, we arrive at the approximate equivalence,

$$I^{H}(t) \approx \left\langle P_{jj}^{H}(t) \right\rangle_{j\in\Psi_0}, \quad (15)$$

which is expected to be valid for a typical initial state. Note that in Equation (15) the average $\left\langle \ldots \right\rangle_{j\in\Psi_0}$ is carried out over the initially occupied sites, i.e., over $1/2$ of all lattice sites, while the average $\left\langle \ldots \right\rangle_{j}$ in Equation (2) is carried out over all lattice sites. The difference between these two definitions of averaging is insignificant, which was numerically confirmed in [23]. This allows us to finally derive Equation (5),

$$I^{H}(t) \approx \left\langle P_{jj}^{H}(t) \right\rangle_{j\in\Psi_0} \approx \left\langle P_{jj}^{H}(t) \right\rangle_{j} = P^{H}(t)\,, \quad (16)$$

which is the main result of this work. We stress that this result is derived considering a single Hamiltonian realization. Still, in the actual numerical calculations in finite systems we also carry out the average over different realizations of Hamiltonians after the quench, $I(t) = \left\langle I^{H}(t) \right\rangle_{H}$ and $P(t) = \left\langle P^{H}(t) \right\rangle_{H}$, such that Equation (16) is rewritten to

$$I(t) \approx P(t)\,. \quad (17)$$

The above result suggests that the time evolution of the particle imbalance from a typical initial product state is approximately identical to the time evolution of the survival probability. The overwhelming majority of eigenstates of $\hat{H}_0$ belong to this category. However, the experimentally relevant initial product states, which form a CDW pattern, do not belong to this category and, hence, they can be considered as atypical states. The evidence for the initial CDW states violating Equation (17) was shown in Ref. [23] for the 1D Aubry–André model at the critical point, at which the exponent of the power-law decay of $I(t)$ did not match the exponent of $P(t)$.

We next test our results numerically. We generate initial states by randomly selecting one of the many-body eigenstates of the initial Hamiltonian $\hat{H}_0$. The overwhelming majority of many-body eigenstates are expected to be typical in the sense defined here. To decrease the effect of rare atypical states, especially for small system sizes, we further average over 50 different Hamiltonian realizations (i.e., over the on-site energies ϵ_i in the 3D Anderson model and over the global phase ϕ in the 1D Aubry–André model).

In Figure 1a,b, we compare $I(t)$ with $P(t)$ for the 3D Anderson model and the 1D Aubry–André model, respectively, at the corresponding eigenstate transition points. We observe that the time evolution of the survival probability $P(t)$ is indeed very close to that of the particle imbalance $I(t)$. The results are nearly indistinguishable for system sizes $L > 4$ for the 3D Anderson model and for system sizes $L > 100$ for the 1D Aubry–André model. In Figures A1 and A2 of Appendix A, we quantify the differences between $I(t)$ and $P(t)$ and we show that the differences decrease with increasing the system size.

As a consequence of similarity between $I(t)$ and $P(t)$ shown in Figure 1, both the rescaled survival probability [20,21] and the rescaled particle imbalance [23] can be used as indicators of critical behavior at the transition point. This observation was the main result of Refs. [20,21,23]; in Appendix B, we summarize how the rescaling of the results in Figure 1 is carried out to detect the critical behavior. We also show in Figure A3 of Appendix B that the exponent of the power-law decay of $I(t)$ in the 1D Aubry–André model for typical initial states considered here matches the exponent of the power-law decay of $P(t)$. This is not the case when considering atypical initial states such as the CDW states [23].

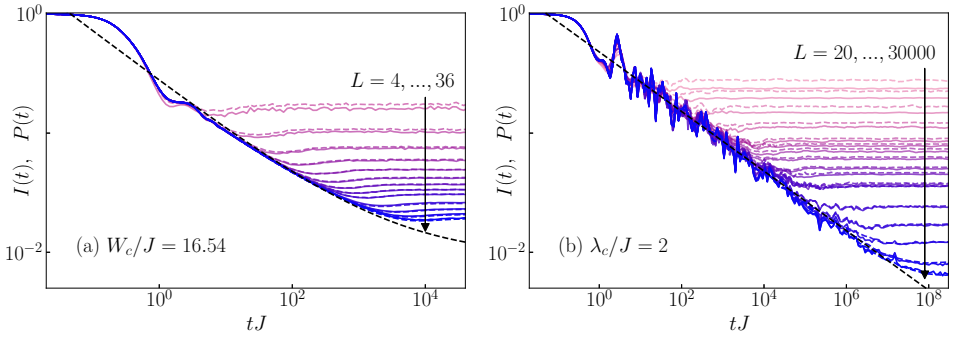

Figure 1. Dynamics of the survival probability $P(t)$ (dashed lines) and particle imbalance $I(t)$ (solid lines), see Equation (17), from the typical initial product states. Results are shown for (**a**) the 3D Anderson model at the critical point $W_c/J = 16.5$ and for system sizes $L = 4, 6, 8, 10, 12, 14, 16, 18, 20, 24, 28, 32, 36$, and (**b**) the 1D Aubry–André model at the critical point $\lambda_c/J = 2$ and for system sizes $L = 20$, 30, 50, 100, 200, 250, 300, 400, 500, 750, 1000, 1250, 2500, 5000, 10,000, 20,000, 30,000. The black dashed line is a fit to the function $a(tJ)^{-\beta} + P_\infty$, where P_∞ is the infinite-time value of $P(t)$ in the thermodynamic limit, which is non-zero (zero) in the case of the 3D Anderson model (1D Aubry–André model) due to the existence (absence) of the mobility edge, see also [20,21].

While the emergence of scale-invariant dynamics of rescaled quantities is limited to the critical point [20,21,23], the similarity between the particle imbalance $I(t)$ and the survival probability $P(t)$, our main result here, also emerges away from the critical point. We show evidence that the similarity between $I(t)$ and $P(t)$ is not restricted to the eigenstate transition point of the 3D Anderson or the 1D Aubry–André model. We compare $I(t)$ to $P(t)$ in the delocalized regime; specifically, for $W/J = 10$ in the 3D Anderson model, see Figure 2a, and for $\lambda/J = 1.98$ in the 1D Aubry–André model, see Figure 3a. We compare $I(t)$ to $P(t)$ in the localized regime; specifically, $W/J = 20$ in the 3D Anderson model, see Figure 2b, and for $\lambda/J = 2.02$ in the 1D Aubry–André model, see Figure 3b. Even though in the 1D Aubry–André model the considered values of λ/J are close to the critical point $\lambda_c/J = 2$, they do not exhibit features of scale-invariant critical dynamics, as demonstrated in Figure A5 of Appendix B. We observe that the time evolution profile of $P(t)$ is still very close to that of the imbalance $I(t)$ in both the delocalized regimes, $W < W_c$ and $\lambda < \lambda_c$, and the localized regimes, $W > W_c$ and $\lambda > \lambda_c$. The agreement occurs despite the two regimes exhibiting distinct dynamical properties. On the one hand, in the delocalized regime at $W/J = 10$ and $\lambda/J = 1.98$, the slope of the decay of $I(t)$ appears to get steeper with the increasing system size and the imbalance decays to zero in the thermodynamic limit, see Figures 2a and 3a, respectively. On the other hand, we observe in the localized regime the decay of $I(t)$ towards the infinite time value $\bar{I}$ that appears to saturate to a nonzero I_∞ in the thermodynamic limit, see Figures 2b and 3b. The insets of Figures 2b and 3b reveal that there is a power-law decay of $I(t) - I_\infty$ (we extract I_∞ in the insets of Figures A4b and A5b), which is analogous to the decay of the survival probability $P(t) - P_\infty$ [20].

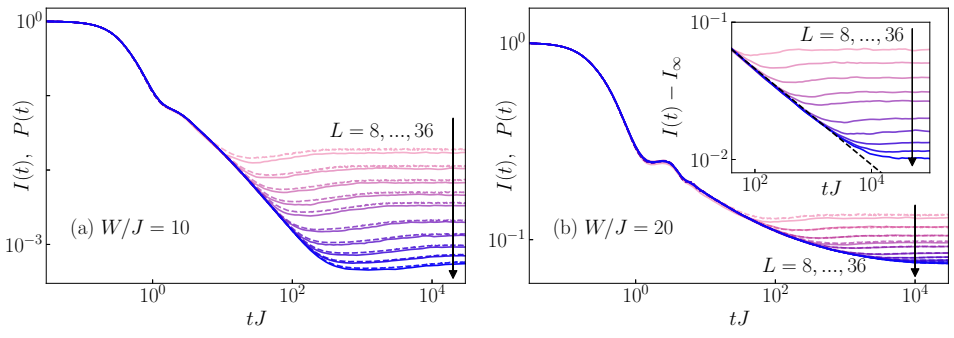

Figure 2. Dynamics of the survival probability $P(t)$ (dashed lines) and particle imbalance $I(t)$ (solid lines), see Equation (17), from the typical initial product states. Results are shown for the 3D Anderson

(**a**) in the delocalized regime $W/J = 10$ and (**b**) in the localized regime $W/J = 20$ for system sizes $L = 8, 10, 12, 14, 16, 20, 24, 28, 32, 36$. Inset of (**b**): subtracted imbalance $I(t) - I_\infty$, which reveals its power-law decay (dashed line). Here, I_∞ is the infinite-time value of $I(t)$ in the thermodynamic limit.

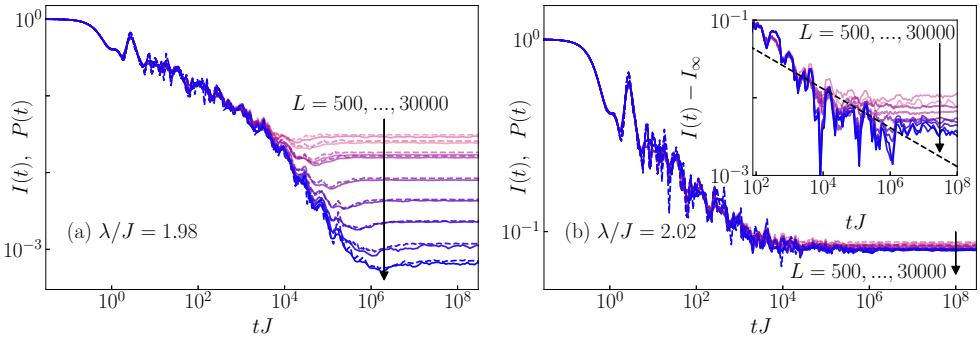

Figure 3. Dynamics of the survival probability $P(t)$ (dashed lines) and particle imbalance $I(t)$ (solid lines), see Equation (17), from the typical initial product states. Results are shown for the 1D Aubry–André model (**a**) in the delocalized regime $\lambda/J = 1.98$ and (**b**) in the localized regime $\lambda/J = 2.02$ for system sizes $L = 500$, 750, 1000, 1250, 2500, 5000, 10,000, 20,000, 30,000. Inset of (**b**): subtracted imbalance $I(t) - I_\infty$, which reveals its power-law decay (dashed line). Here, I_∞ is the infinite-time value of $I(t)$ in the thermodynamic limit.

4. Transition Probabilities and Density Correlation Functions (Generalized Imbalance)

In this section, we generalize the results of Section 3 for the single-particle survival probability to the single-particle transition probabilities between lattice sites i and j at distance d [23],

$$P^{H,(d)}(t) = \Big\langle \sum_{i,|i-j|=d} P^H_{ij}(t) \Big\rangle_j , \tag{18}$$

where $\langle \ldots \rangle_j$ denotes the average over all possible initial states $|j\rangle$, and the distance is defined as the minimal number of hops between the two sites, $|i-j| \equiv ||\mathbf{r}_i - \mathbf{r}_j||_1$. Note that in the limit $d = 0$, we recover the averaged survival probability from Equation (2) since $P^{H,(0)}(t) \equiv P^H(t)$.

It was shown in Ref. [23] that the rescaled transition probabilities exhibit scale-invariant critical dynamics that share certain similarities with the rescaled survival probability. Hence, they can also be applied to detect the eigenstate transitions via quantum dynamics. Here, we search for observables that exhibit similar time evolution profiles as the transition probabilities at $d > 0$.

We argue that the observables of interest are the non-equal time and space density correlation functions at distance d,

$$C^{H,(d)}(t) = \frac{4}{V} \sum_j \sum_{i,|i-j|=d} \Big[\hat{n}^H_i(t) - 1/2\Big] \Big[\hat{n}_j(0) - 1/2\Big] , \tag{19}$$

which can be thought of as the generalization of particle imbalance from Equation (4) since $C^{H,(0)}(t) = I^H(t)$. Hence, we refer to the observable $C^{H,(d)}(t)$ in Equation (19) as the generalized imbalance.

We expect that the time evolution of generalized imbalance, for the typical initial product states discussed in Section 3, is nearly indistinguishable from the time evolution of single-particle transition probabilities,

$$C^{H,(d)}(t) \approx P^{H,(d)}(t) . \tag{20}$$

Equation (20) can be seen as the generalization of Equation (16). The origin of the similarity between the generalized imbalance and transition probabilities is based on the same

argument as the one invoked for the imbalance and survival probabilities in Section 3, i.e., on the self-averaging property of the local environment of lattice sites in the typical initial product states.

Below, we provide numerical evidence for the validity of Equation (20). Specifically, we numerically compare the averages over the Hamiltonian realizations, giving rise to the relationship

$$C^{(d)}(t) \approx P^{(d)}(t)\,, \quad \text{with} \quad C^{(d)}(t) = \langle C^{H,(d)}(t)\rangle_H\,, \quad P^{(d)}(t) = \langle P^{H,(d)}(t)\rangle_H\,. \tag{21}$$

The averages $\langle\ldots\rangle_H$ over Hamiltonian realizations are defined analogously to those in Section 3.

In Figures 4 and 5, we compare $C^{(d)}(t)$ with $P^{(d)}(t)$ for the 3D Anderson model and the 1D Aubry–André model, respectively, at their eigenstate transition points. At $d = 0$, we obtain the results from Section 3 for the imbalance, $C^{(0)}(t) = I(t)$, and the survival probability, $P^{(0)}(t) = P(t)$—compare Figures 4a and 5a to Figure 1a,b, respectively. At $d > 0$, we indeed observe that the time evolution profile of the transition probability $P^{(d)}(t)$ is very close to that of the generalized imbalance $C^{(d)}(t)$. However, with increasing d, larger system sizes L are required to observe the similarity. Therefore, in Figures 4b–d and 5b–d, we only show results for the system sizes at which the agreement is reasonably high. In Figures A1 and A2 of Appendix A, we quantify the differences between $C^{(d)}(t)$ and $P^{(d)}(t)$ and show that they decrease with the increasing system size. In conclusion, the results from this section show that not only the particle imbalance but also the generalized imbalance that corresponds to non-equal time and space density correlations can be made, for typical initial product states, nearly indistinguishable from single-particle quantities, namely, the single-particle transition probabilities between different lattice sites.

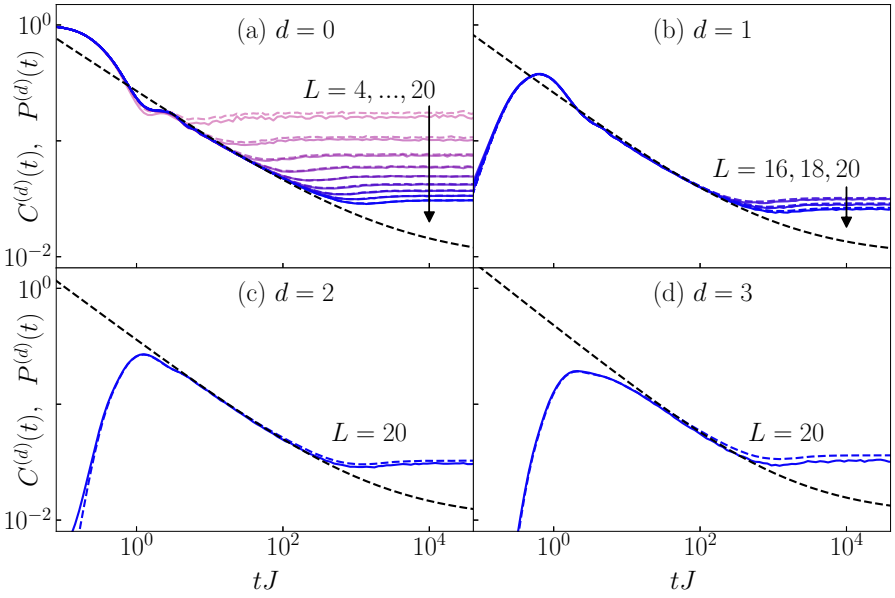

Figure 4. Dynamics of the survival and transition probabilities $P^{(d)}(t)$ (dashed lines) and the corresponding generalized imbalance $C^{(d)}(t)$ (solid lines), see Equation (21), from the typical initial product states. Results are shown for the 3D Anderson model at the critical point $W_c/J = 16.5$ for (**a**) $d = 0$ and $L = 4, 6, 8, 10, 12, 14, 16, 18, 20$, (**b**) $d = 1$ and $L = 16, 18, 20$, (**c**) $d = 2$ and $L = 20$, and (**d**) $d = 3$ and $L = 20$. The black dashed line is a fit to the function $a_d(tJ)^{-\beta_d} + P_\infty^{(d)}$, where $P_\infty^{(d)}$ is the infinite-time value in the thermodynamic limit.

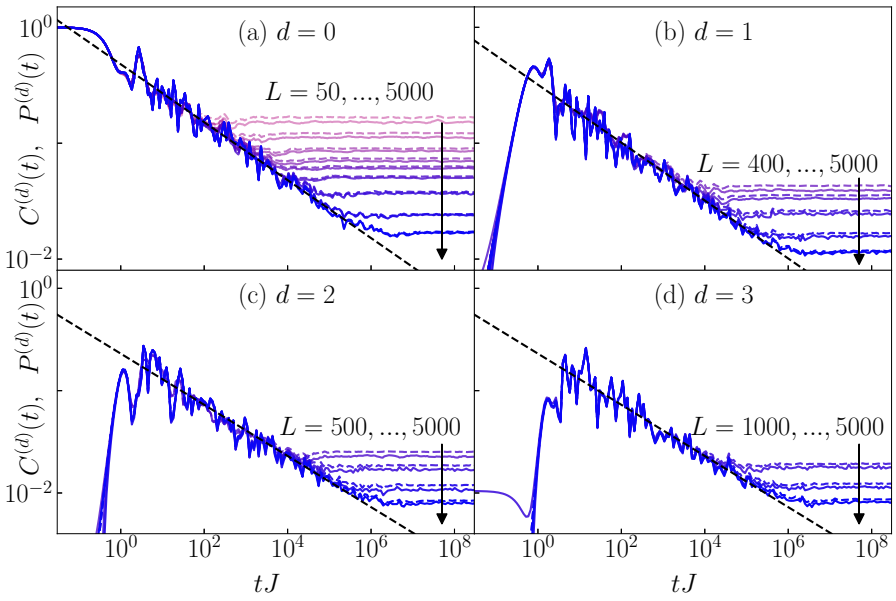

Figure 5. Dynamics of the survival and transition probabilities $P^{(d)}(t)$ (dashed lines) and the corresponding generalized imbalance $C^{(d)}(t)$ (solid lines), see Equation (21), from the typical initial product states. Results are shown for the 1D Aubry–André model at the critical point $\lambda_c/J = 2$ for (**a**) $d = 0$ and $L = 50, 100, 200, 300, 400, 500, 1000, 2500, 5000$, (**b**) $d = 1$ and $L = 400, 500, 1000, 2500, 5000$, (**c**) $d = 2$ and $L = 500, 1000, 2500, 5000$, and (**d**) $d = 3$ and $L = 1000, 2500, 5000$. The black dashed line is a fit to the function $a_d(tJ)^{-\beta_d}$.

5. Equal Time Connected Density–Density Correlation Functions

So far, we have studied the dynamics of particle imbalance, which is a non-equal time density correlation function (4), and the generalized imbalance, which is a non-equal time and space density correlation function (19). We complement these studies by investigating another experimentally relevant quantity [71], i.e., the equal-time connected density–density correlation function [19,72–74]. Even though the dynamics of the latter do not quantitatively agree with the dynamics of single-particle survival or transition probabilities, they still exhibit certain qualitative similarities that we discuss below.

The equal-time connected density–density correlation function is defined as the average of equal-time connected density–density correlations between the sites i and j,

$$C_{eq}^{H,(d)}(t) = \frac{4}{V}\sum_{j}\sum_{i,|i-j|=d} C_{ij}^{H,eq}(t)\,, \tag{22}$$

where the equal-time connected density–density correlation at sites i and j reads

$$C_{ij}^{H,eq}(t) = \langle\Psi_t|\Big[\hat{n}_i - 1/2\Big]\Big[\hat{n}_j - 1/2\Big]|\Psi_t\rangle - \langle\Psi_t|\Big[\hat{n}_i - 1/2\Big]|\Psi_t\rangle\langle\Psi_t|\Big[\hat{n}_j - 1/2\Big]|\Psi_t\rangle\,, \tag{23}$$

and $|\Psi_t\rangle = e^{-i\hat{H}t}|\Psi_0\rangle$. Using Wick's theorem, one can split the density–density correlation term in Equation (23) into two parts [72,73], from which one of them cancels with the second term on the r.h.s. of Equation (23). The remaining term is the product of creation and annihilation operators at different sites, and it can be related to the elements of the one-particle density matrix

$$C_{ij}^{H,eq}(t) = \langle\Psi_t|\hat{c}_i^\dagger\hat{c}_j|\Psi_t\rangle\langle\Psi_t|\hat{c}_i\hat{c}_j^\dagger|\Psi_t\rangle = \rho_{ij}^H(t)\Big[\delta_{ij} - \rho_{ji}^H(t)\Big]\,, \tag{24}$$

where the time-dependent one-particle density matrix is defined as $\rho_{ij}^{H}(t) = \langle \Psi_t | \hat{c}_i^\dagger \hat{c}_j | \Psi_t \rangle$. As a side remark, we note that the matrix elements of the one-particle density matrix can be expressed as

$$\rho_{ij}^{H}(t) = \sum_{j_l \in \Psi_0} [G_{jj_l}^{H}(t)]^* G_{ij_l}^{H}(t) \ , \tag{25}$$

where $G_{jj_l}^{H} = \langle j_l | e^{-i\hat{H}t} | j \rangle$ is the propagator between states $|j\rangle$ and $|j_l\rangle$. One can interpret Equation (25) as the generalization of Equation (8), since the latter reduces to the former at $i = j$.

Before we proceed with the discussion of our numerical results, we first analyze Equation (24). At $d = 0$, the correlations $C_{ii}^{H,eq}(t)$ are non-negative since they can be expressed via the densities as $C_{ii}^{H,eq}(t) = n_i(t) - n_i^2(t)$. Since $n_i(t) \in [0,1]$, it follows that $n_i(t) \geq n_i^2(t)$ and, hence, $C_{ii}^{H,eq}(t) \geq 0$. Moreover, the upper bound $C_{ii}^{H,eq}(t) \leq 1/4$ can be deduced from the same expression. The two bounds then limit the values of the correlation function in Equation (22) at $d = 0$ to the interval $[0,1]$. On the other hand, at $d > 0$, the correlations $C_{ij}^{H,eq}(t)$ are equal to $C_{ij}^{H,eq}(t) = -|\rho_{ij}^{H}(t)|^2$; hence, they are non-positive [72], as is the correlation function in Equation (22). Finally, we also average $C_{eq}^{H,(d)}(t)$ over the Hamiltonian realizations,

$$C_{eq}^{(d)}(t) = \langle C_{eq}^{H,(d)}(t) \rangle_H \ , \tag{26}$$

using the same protocol as in Sections 3 and 4.

Based on the discussion above, in Figure 6, we plot $1 - C_{eq}^{(d)}(t)$ at $d = 0$ and $-C_{eq}^{(d)}(t)$ at $d > 0$, i.e., we plot $\delta_{0,d} - C_{eq}^{(d)}(t)$ instead of $C_{eq}^{(d)}(t)$ that can become negative. Intriguingly, we observe qualitatively similar time evolution profiles as for the survival and transition probabilities. The correlation function $1 - C_{eq}^{(0)}(t)$ exhibits a power-law decay that is qualitatively similar to the decay of the survival probability, compare Figure 6a to Figure 4a and Figure 6e to Figure 5a. In the case of the 3D Anderson model, $1 - C_{eq}^{(0)}(t)$ decays towards a positive constant in the infinite system size limit, see Figure 6a, similarly to the decay of the survival probability to a non-zero constant P_∞. The correlation functions $-C_{eq}^{(d)}(t)$ at $d > 0$ exhibit a maximum after which a power-law decay sets in, which is qualitatively similar to the behavior of the transition probabilities, compare Figure 6b–d to Figure 4b–d and Figure 6f–h to Figure 5b–d. A closer inspection, however, reveals that the slopes of the decay of the equal-time connected density–density correlation functions are larger than in the case of the survival and transition probabilities; hence, in contrast to the results in Sections 3 and 4, a quantitative similarity does not emerge.

The qualitative similarity of the dynamics of the equal-time density–density correlation functions with the dynamics of the survival and transition probabilities motivates us to rescale the former analogously to the rescaling of the latter [20,21]. In Appendices C and D, we show that, indeed, the rescaled equal-time connected density–density correlation functions exhibit scale-invariant mid-time and late-time dynamics, which are similar to the behavior of the survival and transition probabilities [20,21,23]. Thus, the emergence of scale invariance in the dynamics of observables in many-body states appears to be a more general principle that does not necessarily require quantitative similarity with the dynamics of the survival and transition probabilities.

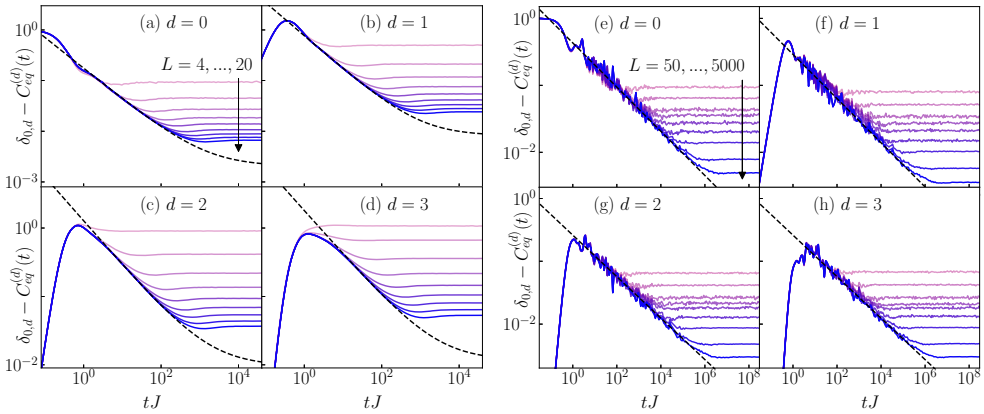

Figure 6. Dynamics of equal-time connected density–density correlation functions $\delta_{0,d} - C_{eq}^{(d)}(t)$, see Equation (26), from the typical initial product states. Results are shown for (**a**–**d**) the 3D Anderson model at the critical point $W_c/J = 16.5$ and for system sizes $L = 4, 6, 8, 10, 12, 14, 16, 18, 20$, and (**e**–**h**) the 1D Aubry–André model at the critical point $\lambda_c/J = 2$ and for system sizes $L = 50, 100, 200, 300, 400, 500, 1000, 2500, 5000$. The black dashed line is a fit to the function $a_d(tJ)^{-\beta_d} + [\delta_{0,d} - C_{eq,\infty}^{(d)}]$, where $[\delta_{0,d} - C_{eq,\infty}^{(d)}]$ is the infinite-time value in the thermodynamic limit, see Appendix C.

6. Discussion

This work focuses on the dynamics of certain one-body observables in many-body states of quadratic fermionic models. We consider quantum quenches in which the initial states are many-body product states on a site occupation basis. In contrast to Ref. [23] that considered initial CDW states, we focused on typical product states with no order in particle occupations. The main conclusions of this work are the following:

(i) We relate the dynamics of particle imbalance to the dynamics of single-particle survival probability, and we show that the two become nearly indistinguishable.

(ii) We extend the result (i) by showing that the generalized imbalance, i.e., the non-equal time and space density correlation function, also becomes nearly indistinguishable from the single-particle transition probabilities. Results (i) and (ii) give a recipe for experiments on how to measure the properties of survival and transition probabilities using one-body observables.

(iii) We discuss the other experimentally relevant observables, i.e., the equal-time connected density–density correlation functions, which can be related to the one-particle density matrix observables. We showed that these observables have qualitative, but not quantitative, similarities with the survival and transition probabilities. Importantly, they also appear to exhibit the scale-invariant dynamics at localization transitions; thus, they constitute an alternative route for the experimental observation of critical dynamics.

Based on our analytical arguments, we expect that the main conclusions listed above are not limited to the two models (the 3D Anderson model and the 1D Aubry–André model) studied numerically in this work.

As the final remark, we note that the most promising quantities for experiments, which allow for the detection of scale-invariant dynamics, are the particle imbalance and the equal-time connected density–density correlation function at distance $d = 0$. The particle imbalance allows one to measure both the scale-invariant critical dynamics and the fractal dimension of the underlying single-particle states but requires the measurement of both $n_i(0)$ and $n_i(t)$. On the other hand, the equal-time connected density–density correlation function at $d = 0$ is a particularly simple quantity since it requires only the measurement of $n_i(t)$.

As an outlook, we give another perspective on the main outcome of this work in Equations (15) and (16). We express the propagator $G_{jj}^H = \langle j|e^{-i\hat{H}t}|j\rangle$ in Equation (1) as a

single-particle Green's function $G^H_{jj} = \langle \Psi_0 | \hat{c}^\dagger_j(t) \hat{c}_j | \Psi_0 \rangle = \langle \Psi_0 | e^{i\hat{H}t} \hat{c}^\dagger_j e^{-i\hat{H}t} \hat{c}_j | \Psi_0 \rangle$ evaluated in the initial many-body state $|\Psi_0\rangle$. Thus, we reformulate Equation (15) as

$$I^H(t) \approx \frac{2}{L} \sum_{j \in \Psi_0} |\langle \Psi_0 | \hat{c}^\dagger_j(t) \hat{c}_j | \Psi_0 \rangle|^2 , \tag{27}$$

which is an expression based purely on single-particle observables in the many-body state. This formulation may motivate future studies, which should explore the validity of Equation (27) for interacting systems that contain non-quadratic terms in the Hamiltonian.

Author Contributions: The computer codes were written and data produced by M.H. Both authors contributed to the data analysis and writing of the paper. All authors have read and agreed to the published version of the manuscript.

Funding: This work was supported by the Slovenian Research and Innovation Agency (ARIS), Research core fundings Grants No. P1-0044, N1-0273 and J1-50005. We gratefully acknowledge the High Performance Computing Research Infrastructure Eastern Region (HCP RIVR) consortium [75] and European High Performance Computing Joint Undertaking (EuroHPC JU) [76] for funding this research by providing computing resources of the HPC system Vega at the Institute of Information Sciences [77].

Institutional Review Board Statement: Not applicable.

Data Availability Statement: All data are available upon request.

Acknowledgments: We acknowledge discussions with F. Heidrich-Meisner, S. Jiricek, and P. Łydżba.

Conflicts of Interest: The authors declare no conflicts of interest.

Appendix A. System Size Dependence of Differences between $P^{(d)}$ and $C^{(d)}$

Here, we quantify the differences between the transition probabilities $P^{(d)}$ and the generalized imbalances $C^{(d)}$ from Equation (21), defined by their absolute differences,

$$\sigma^{(d)}_{\text{abs}}(t) = |C^{(d)}(t) - P^{(d)}(t)| . \tag{A1}$$

At $d = 0$, Equation (A1) reduces to the differences between the survival probabilities $P = P^{(0)}$ and the particle imbalance $I = C^{(0)}$, as discussed in Section 3.

In Figures A1a–d and A2a–d, we show $\sigma^{(d)}_{\text{abs}}(t)$ for the 3D Anderson model and the 1D Aubry–André model, respectively. We observe a decrease in the differences with the system size. To quantify the system size dependence of the differences, we first perform their time averages defined as

$$\overline{\sigma^{(d)}_{\text{abs}}(t)} = \frac{1}{N_t} \sum_{\{t_i\}} \sigma^{(d)}_{\text{abs}}(t_i) , \tag{A2}$$

where N_t is the number of values in the discrete time set $\{t_i\}$. For the averages, we consider only times larger than $tJ = 10^1$ and $tJ = 10^2$ for the 3D Anderson model and the 1D Aubry–André model, respectively, at which the differences approach their steady-state values. The vertical dotted lines in Figures A1a–d and A2a–d denote the onset of the steady-state behavior.

In Figures A1e and A2e, we plot $\overline{\sigma^{(d)}_{\text{abs}}(t)}$ as a function of the number of lattice sites for the 3D Anderson model and the 1D Aubry–André model, respectively. The results are consistent with a power-law decay. We perform a fit to the results of form aL^{-b}, where a and b are fitting parameters. For the 3D Anderson model, we find $b \approx 3$, and for the 1D Aubry–André model, we find $b \approx 1$, which suggests that in both cases the differences vanish upon increasing the system size.

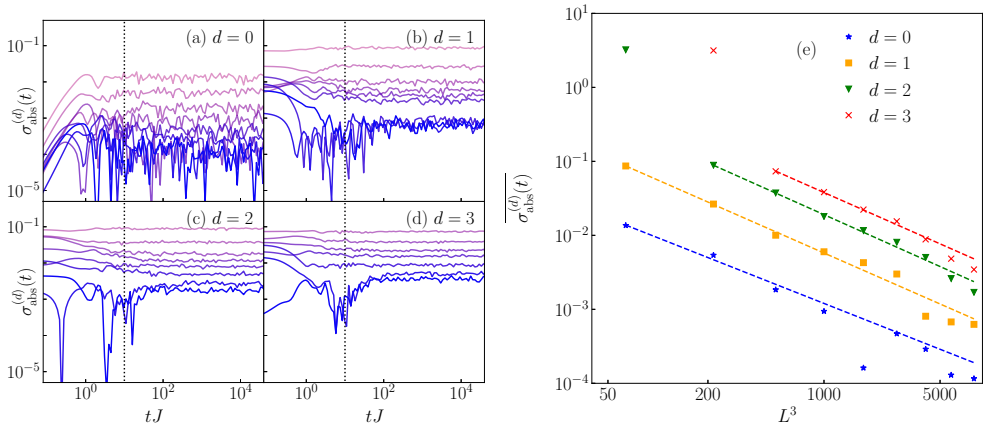

Figure A1. The absolute differences $\sigma^{(d)}_{\rm abs}(t)$ for (**a**) $d = 0$, (**b**) $d = 1$, (**c**) $d = 2$, and (**d**) $d = 3$ for the 3D Anderson model at the critical point $W_c/J = 16.5$ and for system sizes $L = 4, 6, 8, 10, 12, 14, 16, 18, 20$, corresponding to the results in Figures 1a and 4. Panel (**e**) displays the averaged absolute differences $\overline{\sigma^{(d)}_{\rm abs}(t)}$ as a function of system volume L^3. The averaging is performed over times larger than $tJ = 10$ (dotted vertical lines in panels (**a**–**d**)). The dashed lines in panel (**e**) are fits to the results of form aL^{-b}.

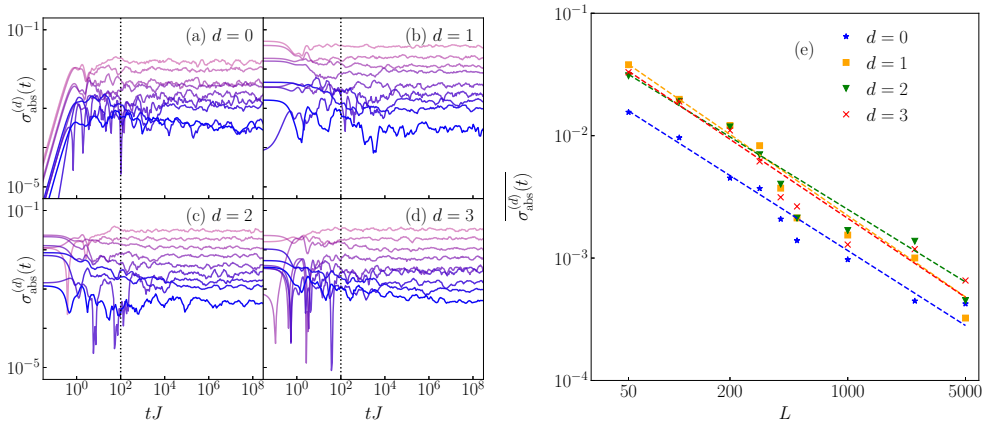

Figure A2. The absolute differences $\sigma^{(d)}_{\rm abs}(t)$ for (**a**) $d = 0$, (**b**) $d = 1$, (**c**) $d = 2$, and (**d**) $d = 3$ for the 1D Aubry–André model at the critical point $\lambda_c/J = 2$ and for system sizes $L = 50, 100, 200, 300, 400, 500, 1000, 2500, 5000$, corresponding to the results in Figures 1b and 5. Panel (**e**) displays the averaged absolute differences $\overline{\sigma^{(d)}_{\rm abs}(t)}$ as a function of system size L. The averaging is performed over times larger than $tJ = 10^2$ (dotted vertical lines in panels (**a**–**d**)). The dashed lines in panel (**e**) are fits to the results of form aL^{-b}.

Appendix B. Rescaled Imbalance and Transition Probabilities: Scale-Invariant Dynamics at Eigenstate Transitions

Motivated by Refs. [20,21,23], we perform rescaling of the results for particle imbalance in Figures 1–3. As the dynamics of particle imbalance are nearly indistinguishable from the dynamics of survival probability, the originally proposed rescaling for the survival probability in Refs. [20,21] reduces to the rescaling of the imbalance proposed in Ref. [23]. The rescaled imbalance [23] is defined as

$$\tilde{I}(\tau) = \frac{I(\tau) - I_\infty}{\bar{I} - I_\infty}\,, \tag{A3}$$

where the infinite-time value at a fixed system size reads $\bar{I} = \lim_{t\to\infty} I(t)$, and the corresponding value in the thermodynamic limit I_∞ is extracted from the power-law decay ansatz,

$$\bar{I} = c_I\, D^{-\gamma_I} + I_\infty\,, \tag{A4}$$

where $D = V$ is the single-particle Hilbert space dimension. Fits of the results to this ansatz are shown in the insets of Figures A3–A5. The scaled time τ is measured in units of the typical Heisenberg time t_H^{typ},

$$\tau = t/t_H^{\text{typ}}\,, \quad t_H^{\text{typ}} = 2\pi\, \mathrm{e}^{-\langle\langle \ln(\varepsilon_{q+1}-\varepsilon_q)\rangle_q\rangle_H}\,, \tag{A5}$$

in which $\langle\ldots\rangle_q$ denotes the average over all neighboring single-particle eigenenergies ε_q of $\hat{H}$ and $\langle\ldots\rangle_H$ is the average over Hamiltonian realizations.

In Figure A3a,b, we plot the rescaled imbalance $\tilde{I}(\tau)$ for the 3D Anderson model and the 1D Aubry–André model at their critical points, respectively. The data in Figure A3 are identical to those in Figure 1. We observe clear emergence of scale invariance in the critical dynamics of the particle imbalance, which is consistent with the results for the survival probability in Ref. [20].

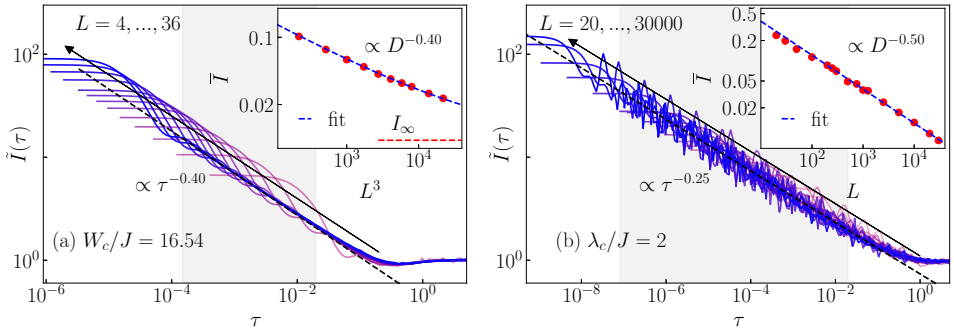

Figure A3. Dynamics of the rescaled particle imbalance $\tilde{I}(\tau)$ as a function of scaled time τ, see Equation (A3). Data are the same as in Figure 1, and they are shown for (**a**) the 3D Anderson model at the critical point $W_c/J = 16.5$ and for system sizes $L = 4, 6, 8, 10, 12, 14, 16, 18, 20, 24, 28, 32, 36$, and (**b**) the 1D Aubry–André model at the critical point $\lambda_c/J = 2$ and for system sizes L = 20, 30, 50, 100, 200, 250, 300, 400, 500, 750, 1000, 1250, 2500, 5000, 10,000, 20,000, 30,000. The dashed line is a two-parameter fit (within the shaded regions) to the function $\tilde{I}(\tau) = a_I\, \tau^{-\beta_I}$. Inset: Infinite-time values $\bar{I}$ versus the single-particle Hilbert-space dimension $D = L^3$ (circles) and the three-parameter fits to Equation (A4) (dashed line). The horizontal dashed line is the infinite-time value in the thermodynamic limit I_∞.

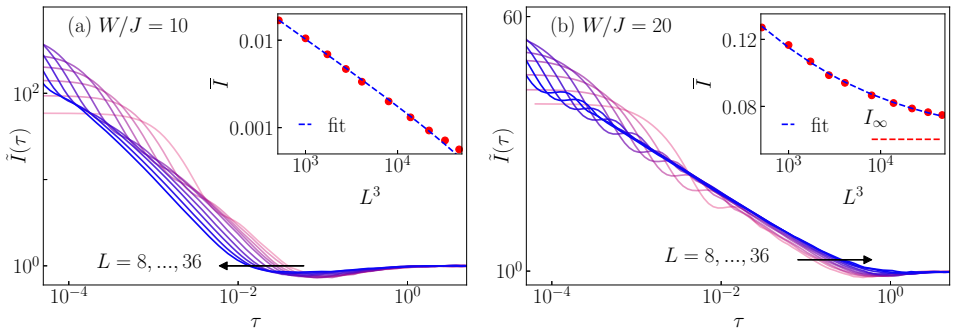

Figure A4. Dynamics of the rescaled particle imbalance $\tilde{I}(\tau)$ as a function of scaled time τ, see Equation (A3). Data are the same as in Figure 2, and they are shown for the 3D Anderson model (**a**) in the delocalized regime $W/J = 10$ and (**b**) in the localized regime $W/J = 20$ for system sizes $L = 8, 10, 12, 14, 16, 20, 24, 28, 32, 36$. Inset: Infinite-time values $\bar{I}$ versus the single-particle Hilbert-space dimension $D = L^3$ (circles) and the three-parameter fits to Equation (A4) (dashed line). The horizontal dashed line is the infinite-time value in the thermodynamic limit I_∞.

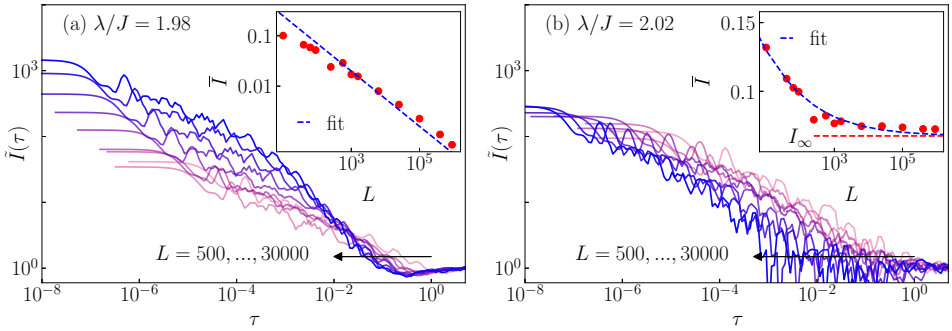

Figure A5. Dynamics of the rescaled particle imbalance $\tilde{I}(\tau)$ as a function of scaled time τ, see Equation (A3). Data are the same as in Figure 3, and they are shown for the 1D Aubry–André model (**a**) in the delocalized regime $\lambda/J = 1.98$ and (**b**) in the localized regime $\lambda/J = 2.02$ for system sizes L = 500, 750, 1000, 1250, 2500, 5000, 10,000, 20,000, 30,000. Inset: Infinite-time values $\bar{I}$ versus the single-particle Hilbert-space dimension $D = L$ (circles) and the three-parameter fits to Equation (A4) (dashed line). The horizontal dashed line is the infinite-time value in the thermodynamic limit I_∞.

We note that the scale-invariant dynamics at the critical point was also shown to emerge for the transition probabilities $P^{(d)}(t)$ from Equation (21), see Ref. [23]. Hence, since the generalized imbalance $C^{(d)}(t)$ from Equation (21) becomes nearly indistinguishable from the transition probability $P^{(d)}(t)$, we expect that $C^{(d)}(t)$ ultimately develops the scale invariance as well. However, this is only expected to occur for very large system sizes; therefore, the generalized imbalances $C^{(d)}(t)$ for $d > 0$ are less useful for the experimental detection of scale invariance than the particle imbalance. Thus, we do not explicitly discuss here the rescaling of $C^{(d)}(t)$ for $d > 0$.

In Figures A4 and A5, we show the rescaled imbalance $\tilde{I}(\tau)$ in the 3D Anderson model and 1D Aubry–André model, respectively, at the two disorder strengths away from the critical point. The data in Figures A4a and A5a are identical to those in Figures 2a and 3a, respectively, and the data in Figures A4b and A5b are identical to those in Figures 2b and 3b, respectively. In all cases, we do not observe indications of scale invariance. In the 3D Anderson model at $W/J = 10$, the decay as a function of τ becomes faster with increasing L, see Figure A4a, which complies with the relaxation time shorter than the typical Heisenberg time [40]. Conversely, at $W/J = 20$, the relaxation time is larger than the Heisenberg time [40], which results in the opposite drifts of the curves with the system size [23], see Figure A4b. In the 1D Aubry–André model at $\lambda/J = 1.98$, the decay as a function of τ becomes faster with increasing L, see Figure A5a, again indicating relaxation at times shorter than the typical Heisenberg time. At $\lambda/J = 2.02$, the relaxation also occurs at times shorter than the typical Heisenberg time, see Figure A5b, which causes the scaled imbalance $\tilde{I}(\tau)$ to shift to the left with increasing L. Hence, while the rescaled imbalance exhibits scale-invariant critical dynamics at the eigenstate transition points, this does not appear to be the case away from it.

Appendix C. Equal-Time Connected Density–Density Correlation Functions: Scale-Invariant Dynamics at Eigenstate Transitions

Interestingly, even though the dynamics of the equal-time connected density–density correlation functions $C_{eq}^{(d)}(t)$ are not quantitatively related to the dynamics of the survival and transition probabilities, when rescaled, they develop scale invariance analogous to those discussed in Appendix B. Indeed, it was argued in Ref. [23] that the scale invariance at the eigenstate transition is not limited to the observables that become indistinguishable from the survival or transition probabilities; hence, the emergence of scale invariance can be considered as a general principle. Here, we follow this principle and we perform a rescaling,

analogous to the rescaling in Equation (A3), of the equal-time connected density–density correlations functions from Section 5. The rescaling is defined as

$$\tilde{C}_{eq}^{(d)}(\tau) = \frac{C_{eq}^{(d)}(\tau) - C_{eq,\infty}^{(d)}}{\overline{C}_{eq}^{(d)} - C_{eq,\infty}^{(d)}}\,, \tag{A6}$$

where the infinite-time values read $\overline{C}_{eq}^{(d)} = \lim_{t\to\infty} C_{eq}^{(d)}(t)$. The thermodynamic limit of $\overline{C}_{eq}^{(d)}$ is extracted from the power-law decay ansatz

$$\overline{C}_{eq}^{(d)} = c_C^{(d)}\, D^{-\gamma_C^{(d)}} + C_{eq,\infty}^{(d)}\,. \tag{A7}$$

In Figures A6a–d and A7a–d, we plot the rescaled equal-time connected density–density correlation functions $\tilde{C}_{eq}^{(d)}(\tau)$ for the 3D Anderson model and the 1D Aubry–André model at their critical points, respectively. We observe the emergence of scale invariance in all panels.

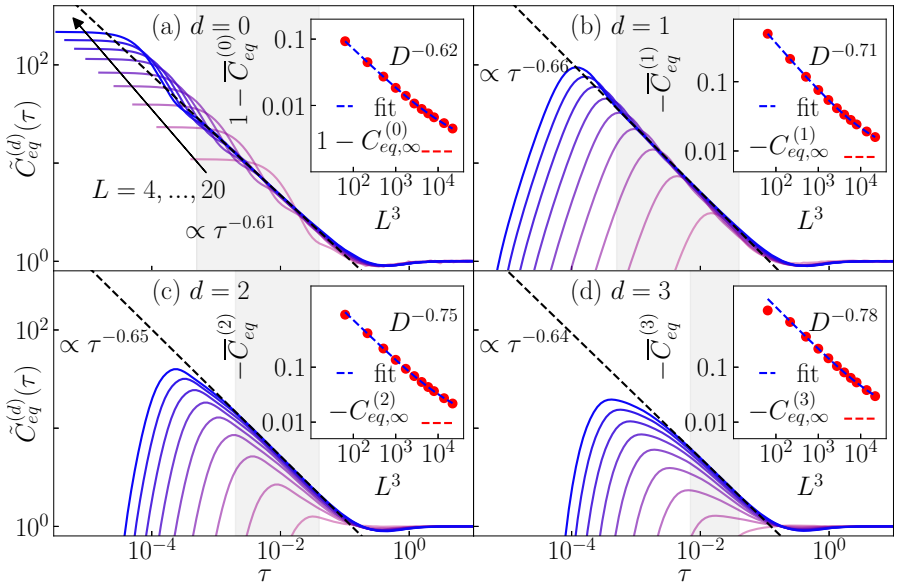

Figure A6. Dynamics of the rescaled equal-time connected density–density correlation functions $\tilde{C}_{eq}^{(d)}(\tau)$, see Equation (A6), from the typical initial product states. Results are shown for the 3D Anderson model at the critical point $W_c/J = 16.5$ and for system sizes $L = 4, 6, 8, 10, 12, 14, 16, 18, 20$. The dashed line is a two-parameter fit (within the shaded regions) to the power-law decay from Equation (A8). Inset: Infinite-time values $\delta_{0,d} - \overline{C}_{eq}^{(0)}$ versus the single-particle Hilbert-space dimension $D = L^3$ (circles) and the three-parameter fits to Equation (A7) (dashed line). The horizontal dashed line is the infinite-time value in the thermodynamic limit $\delta_{0,d} - C_{eq,\infty}^{(d)}$.

Another property that can be observed from Figure A6 is that the decay follows a power-law,

$$\tilde{C}_{eq}^{(d)}(\tau) = a_C^{(d)} \tau^{-\beta_C^{(d)}}\,. \tag{A8}$$

The power-law exponent $\beta_C^{(d)}$ is generally larger than the corresponding exponent for the transition probability β_d [23]. In the case of the 3D Anderson model, the values of β_d for $d \in \{0, 1, 2, 3\}$ are in range $\beta_d \in [0.4, 0.45]$ [23] and the corresponding values of $\beta_C^{(d)}$ in Figure A6a–d are in range $\beta_C^{(d)} \in [0.61, 0.66]$. It remains an open question as to whether the variations in values of $\beta_C^{(d)}$ for different d are caused by finite size effects, converging ultimately to the same value in the thermodynamic limit, or they will remain distinct. In

the 1D Aubry–André model, the former scenario appears to be more plausible since we obtain $\beta_d \approx 0.26$ for all d [23] and $\beta_C^{(d)} \approx 0.33$ for all d in Figure A7.

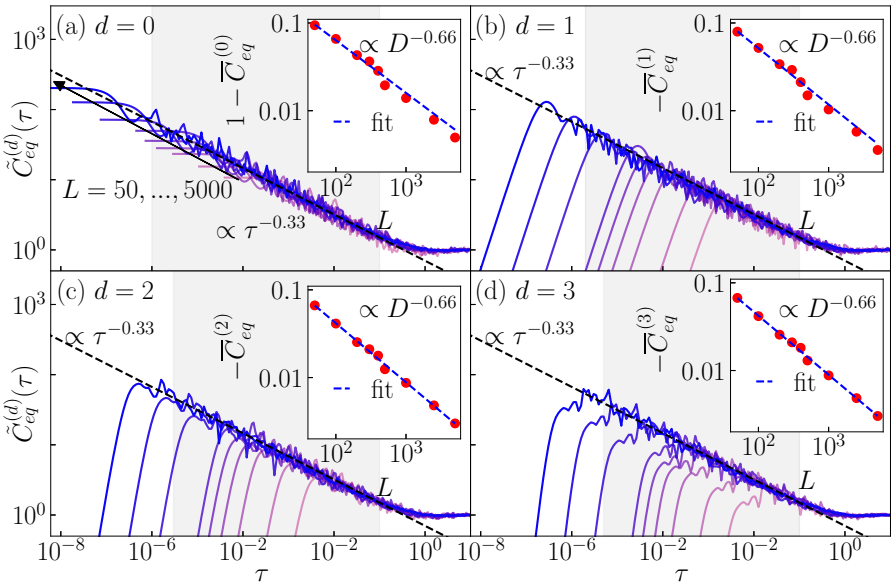

Figure A7. Dynamics of the rescaled equal-time connected density–density correlation functions $\tilde{C}_{eq}^{(d)}(\tau)$, see Equation (A6), from the typical initial product states. Results are shown for the 1D Aubry–André model at the critical point $\lambda_c/J = 2$ and for system sizes $L = 50, 100, 200, 300, 400, 500, 1000, 2500, 5000$. The dashed line is a two-parameter fit (within the shaded regions) to the power-law decay from Equation (A8). Inset: Infinite-time values $\delta_{0,d} - \overline{C}_{eq}^{(0)}$ versus the single-particle Hilbert-space dimension $D = L$ (circles) and the three-parameter fits to Equation (A7) (dashed line).

Appendix D. Connection to Fractal Dimension

Finally, let us comment on the relationship between the power-law exponents β and the fractal dimension. In Refs. [20,21], it was established that the power-law exponent β of the decay of survival probability is related to the fractal dimension γ, which is defined via the finite-size scaling of the inverse participation ratio (see Refs. [20,21] for details). The precise relation is given by $\gamma = n\beta$, where n determines the scaling of the typical Heisenberg time with the system size at the critical point, $t_H^{\text{typ}} = D^n$ ($n \approx 1$ in the 3D Anderson model and $n \approx 2$ in the 1D Aubry–André model [20]). If the dynamics of particle imbalance are nearly identical to the dynamics of survival probability, as in the case studied here for the typical initial product states, then one should expect the analogous relation $\gamma_I = n\beta_I$ with $\gamma_I = \gamma$ and $\beta_I = \beta$. Note that in Ref. [23], the relation $\gamma_I = n\beta_I$ was found even for the initial CDW states. However, while for the initial CDW states it was observed that $\gamma_I \approx \gamma$ in the 3D Anderson model, it was also observed that $\gamma_I \neq \gamma$ in the 1D Aubry–André model.

Here, we check for both models whether a similar relation also holds true for the equal-time connected density–density correlation functions,

$$\gamma_C^{(d)} = n\beta_C^{(d)}. \tag{A9}$$

Numerical results for $\beta_C^{(d)}$ are shown in the main panels of Figures A6 and A7, while the numerical results for $\gamma_C^{(d)}$ are shown in the corresponding insets. For the 1D Aubry–André model, the relation in Equation (A9) is valid up to the second decimal digit for all d, as can be seen from Figure A7. In the case of the 3D Anderson model, the relation in Equation (A9) is valid almost up to the second digit for $d = 0$, see Figure A6a, but it deteriorates when d is increased, see Figure A6b–d. We checked that a similar agreement is observed also for the

transition probabilities. We believe that the deviations at large d are finite size effects since the numerical calculation of the slopes requires two fitting procedures, for which the results get less predictive as we increase d while keeping L the same. The validity of Equation (A9) may be interpreted as being a consequence of the scale-invariant power-law behavior.

References

1. Ketzmerick, R.; Petschel, G.; Geisel, T. Slow decay of temporal correlations in quantum systems with Cantor spectra. *Phys. Rev. Lett.* **1992**, *69*, 695–698. [CrossRef] [PubMed]
2. Huckestein, B.; Schweitzer, L. Relation between the correlation dimensions of multifractal wave functions and spectral measures in integer quantum Hall systems. *Phys. Rev. Lett.* **1994**, *72*, 713–716. [CrossRef] [PubMed]
3. Schofield, S.A.; Wolynes, P.G.; Wyatt, R.E. Computational Study of Many-Dimensional Quantum Energy Flow: From Action Diffusion to Localization. *Phys. Rev. Lett.* **1995**, *74*, 3720–3723. [CrossRef] [PubMed]
4. Schofield, S.A.; Wyatt, R.E.; Wolynes, P.G. Computational study of many-dimensional quantum vibrational energy redistribution. I. Statistics of the survival probability. *J. Chem. Phys.* **1996**, *105*, 940–952. [CrossRef]
5. Brandes, T.; Huckestein, B.; Schweitzer, L. Critical dynamics and multifractal exponents at the Anderson transition in 3d disordered systems. *Ann. Phys.* **1996**, *508*, 633–651. [CrossRef]
6. Ketzmerick, R.; Kruse, K.; Kraut, S.; Geisel, T. What Determines the Spreading of a Wave Packet? *Phys. Rev. Lett.* **1997**, *79*, 1959–1963. [CrossRef]
7. Ohtsuki, T.; Kawarabayashi, T. Anomalous Diffusion at the Anderson Transitions. *J. Phys. Soc. Jpn.* **1997**, *66*, 314–317. [CrossRef]
8. Gruebele, M. Intramolecular vibrational dephasing obeys a power law at intermediate times. *Proc. Natl. Acad. Sci. USA* **1998**, *95*, 5965–5970. [CrossRef]
9. Ng, G.S.; Bodyfelt, J.; Kottos, T. Critical Fidelity at the Metal-Insulator Transition. *Phys. Rev. Lett.* **2006**, *97*, 256404. [CrossRef]
10. Torres-Herrera, E.J.; Santos, L.F. Local quenches with global effects in interacting quantum systems. *Phys. Rev. E* **2014**, *89*, 062110. [CrossRef]
11. Torres-Herrera, E.J.; Santos, L.F. Dynamics at the many-body localization transition. *Phys. Rev. B* **2015**, *92*, 014208. [CrossRef]
12. Leitner, D.M. Quantum ergodicity and energy flow in molecules. *Adv. Phys.* **2015**, *64*, 445–517. [CrossRef]
13. Santos, L.F.; Torres-Herrera, E.J. Analytical expressions for the evolution of many-body quantum systems quenched far from equilibrium. *AIP Conf. Proc.* **2017**, *1912*, 020015. [CrossRef]
14. Torres-Herrera, E.J.; García-García, A.M.; Santos, L.F. Generic dynamical features of quenched interacting quantum systems: Survival probability, density imbalance, and out-of-time-ordered correlator. *Phys. Rev. B* **2018**, *97*, 060303. [CrossRef]
15. Bera, S.; De Tomasi, G.; Khaymovich, I.M.; Scardicchio, A. Return probability for the Anderson model on the random regular graph. *Phys. Rev. B* **2018**, *98*, 134205. [CrossRef]
16. Prelovšek, P.; Barišić, O.S.; Mierzejewski, M. Reduced-basis approach to many-body localization. *Phys. Rev. B* **2018**, *97*, 035104. [CrossRef]
17. Schiulaz, M.; Torres-Herrera, E.J.; Santos, L.F. Thouless and relaxation time scales in many-body quantum systems. *Phys. Rev. B* **2019**, *99*, 174313. [CrossRef]
18. Karmakar, S.; Keshavamurthy, S. Intramolecular vibrational energy redistribution and the quantum ergodicity transition: A phase space perspective. *Phys. Chem. Chem. Phys.* **2020**, *22*, 11139–11173. [CrossRef] [PubMed]
19. Lezama, T.L.M.; Torres-Herrera, E.J.; Pérez-Bernal, F.; Bar Lev, Y.; Santos, L.F. Equilibration time in many-body quantum systems. *Phys. Rev. B* **2021**, *104*, 085117. [CrossRef]
20. Hopjan, M.; Vidmar, L. Scale-Invariant Survival Probability at Eigenstate Transitions. *Phys. Rev. Lett.* **2023**, *131*, 060404. [CrossRef]
21. Hopjan, M.; Vidmar, L. Scale-invariant critical dynamics at eigenstate transitions. *Phys. Rev. Res.* **2023**, *5*, 043301. [CrossRef]
22. Das, A.K.; Pinney, P.; Zarate-Herrada, D.A.; Pilatowsky-Cameo, S.; Matsoukas-Roubeas, A.S.; Cabral, D.G.A.; Cianci, C.; Batista, V.S.; del Campo, A.; Torres-Herrera, E.J.; et al. Proposal for many-body quantum chaos detection. *arXiv* **2024**, arXiv:2401.01401.
23. Jiricek, S.; Hopjan, M.; Łydżba, P.; Heidrich-Meisner, F.; Vidmar, L. Critical quantum dynamics of observables at eigenstate transitions. *Phys. Rev. B* **2024**, *109*, 205157. [CrossRef]
24. Schreiber, M.; Hodgman, S.S.; Bordia, P.; Lüschen, H.P.; Fischer, M.H.; Vosk, R.; Altman, E.; Schneider, U.; Bloch, I. Observation of many-body localization of interacting fermions in a quasirandom optical lattice. *Science* **2015**, *349*, 842–845. [CrossRef]
25. Choi, J.Y.; Hild, S.; Zeiher, J.; Schauß, P.; Rubio-Abadal, A.; Yefsah, T.; Khemani, V.; Huse, D.A.; Bloch, I.; Gross, C. Exploring the many-body localization transition in two dimensions. *Science* **2016**, *352*, 1547–1552. [CrossRef]
26. Lüschen, H.P.; Bordia, P.; Scherg, S.; Alet, F.; Altman, E.; Schneider, U.; Bloch, I. Observation of Slow Dynamics near the Many-Body Localization Transition in One-Dimensional Quasiperiodic Systems. *Phys. Rev. Lett.* **2017**, *119*, 260401. [CrossRef]
27. Bordia, P.; Lüschen, H.; Scherg, S.; Gopalakrishnan, S.; Knap, M.; Schneider, U.; Bloch, I. Probing Slow Relaxation and Many-Body Localization in Two-Dimensional Quasiperiodic Systems. *Phys. Rev. X* **2017**, *7*, 041047. [CrossRef]
28. Kohlert, T.; Scherg, S.; Li, X.; Lüschen, H.P.; Das Sarma, S.; Bloch, I.; Aidelsburger, M. Observation of Many-Body Localization in a One-Dimensional System with a Single-Particle Mobility Edge. *Phys. Rev. Lett.* **2019**, *122*, 170403. [CrossRef]
29. Rubio-Abadal, A.; Choi, J.Y.; Zeiher, J.; Hollerith, S.; Rui, J.; Bloch, I.; Gross, C. Many-Body Delocalization in the Presence of a Quantum Bath. *Phys. Rev. X* **2019**, *9*, 041014. [CrossRef]

30. Guo, Q.; Cheng, C.; Sun, Z.H.; Song, Z.; Li, H.; Wang, Z.; Ren, W.; Dong, H.; Zheng, D.; Zhang, Y.R.; et al. Observation of energy-resolved many-body localization. *Nat. Phys.* **2021**, *17*, 234–239. [CrossRef]
31. Pöpperl, P.; Gornyi, I.V.; Mirlin, A.D. Memory effects in the density-wave imbalance in delocalized disordered systems. *Phys. Rev. B* **2022**, *106*, 094201. [CrossRef]
32. Anderson, P.W. Absence of Diffusion in Certain Random Lattices. *Phys. Rev.* **1958**, *109*, 1492–1505. [CrossRef]
33. Abrahams, E.; Anderson, P.W.; Licciardello, D.C.; Ramakrishnan, T.V. Scaling Theory of Localization: Absence of Quantum Diffusion in Two Dimensions. *Phys. Rev. Lett.* **1979**, *42*, 673–676. [CrossRef]
34. Evers, F.; Mirlin, A.D. Anderson transitions. *Rev. Mod. Phys.* **2008**, *80*, 1355–1417. [CrossRef]
35. Aubry, S.; André, G. Analyticity breaking and Anderson localization in incommensurate lattices. *Ann. Isr. Phys. Soc.* **1980**, *3*, 18.
36. Suslov, I. Anderson Localization in Incommensurate Systems. *J. Exp. Theor. Phys.* **1982**, *56*, 612.
37. Kramer, B.; MacKinnon, A. Localization: Theory and experiment. *Rep. Prog. Phys.* **1993**, *56*, 1469–1564. [CrossRef]
38. Brandes, T.; Kettemann, S. *Anderson Localization and Its Ramifications: Disorder, Phase Coherence, and Electron Correlations*; Lecture Notes in Physics; Springer: Berlin/Heidelberg, Germany, 2003.
39. Lagendijk, A.; Tiggelen, B.V.; Wiersma, D.S. Fifty years of Anderson localization. *Phys. Today* **2009**, *62*, 24–29. [CrossRef]
40. Šuntajs, J.; Prosen, T.; Vidmar, L. Spectral properties of three-dimensional Anderson model. *Ann. Phys.* **2021**, *435*, 168469. [CrossRef]
41. MacKinnon, A.; Kramer, B. One-Parameter Scaling of Localization Length and Conductance in Disordered Systems. *Phys. Rev. Lett.* **1981**, *47*, 1546–1549. [CrossRef]
42. MacKinnon, A.; Kramer, B. The scaling theory of electrons in disordered solids: Additional numerical results. *Z. Phys. B* **1983**, *53*, 1–13. [CrossRef]
43. Tarquini, E.; Biroli, G.; Tarzia, M. Critical properties of the Anderson localization transition and the high-dimensional limit. *Phys. Rev. B* **2017**, *95*, 094204. [CrossRef]
44. Slevin, K.; Ohtsuki, T. Critical Exponent of the Anderson Transition Using Massively Parallel Supercomputing. *J. Phys. Soc. Jpn.* **2018**, *87*, 094703. [CrossRef]
45. Zhao, Y.; Feng, D.; Hu, Y.; Guo, S.; Sirker, J. Entanglement dynamics in the three-dimensional Anderson model. *Phys. Rev. B* **2020**, *102*, 195132. [CrossRef]
46. Prelovšek, P.; Herbrych, J. Diffusion in the Anderson model in higher dimensions. *Phys. Rev. B* **2021**, *103*, L241107. [CrossRef]
47. Rodriguez, A.; Vasquez, L.J.; Römer, R.A. Multifractal Analysis with the Probability Density Function at the Three-Dimensional Anderson Transition. *Phys. Rev. Lett.* **2009**, *102*, 106406. [CrossRef]
48. Rodriguez, A.; Vasquez, L.J.; Slevin, K.; Römer, R.A. Critical Parameters from a Generalized Multifractal Analysis at the Anderson Transition. *Phys. Rev. Lett.* **2010**, *105*, 046403. [CrossRef]
49. Schubert, G.; Weiße, A.; Wellein, G.; Fehske, H. HQS@HPC: Comparative numerical study of Anderson localisation in disordered electron systems. In Proceedings of the High Performance Computing in Science and Engineering, Garching, Germany, 14–15 October 2004; Bode, A., Durst, F., Eds.; Springer: Berlin/Heidelberg, Germany, 2005; pp. 237–249.
50. Li, X.; Pixley, J.H.; Deng, D.L.; Ganeshan, S.; Das Sarma, S. Quantum nonergodicity and fermion localization in a system with a single-particle mobility edge. *Phys. Rev. B* **2016**, *93*, 184204. [CrossRef]
51. Hopjan, M.; Orso, G.; Heidrich-Meisner, F. Detecting delocalization-localization transitions from full density distributions. *Phys. Rev. B* **2021**, *104*, 235112. [CrossRef]
52. Bhakuni, D.S.; Lev, Y.B. Dynamic scaling relation in quantum many-body systems. *Phys. Rev. B* **2024**, *110*, 014203. [CrossRef]
53. Domínguez-Castro, G.A.; Paredes, R. The Aubry–André model as a hobbyhorse for understanding the localization phenomenon. *Eur. J. Phys.* **2019**, *40*, 045403. [CrossRef]
54. Kohmoto, M. Metal-Insulator Transition and Scaling for Incommensurate Systems. *Phys. Rev. Lett.* **1983**, *51*, 1198–1201. [CrossRef]
55. Tang, C.; Kohmoto, M. Global scaling properties of the spectrum for a quasiperiodic schrödinger equation. *Phys. Rev. B* **1986**, *34*, 2041–2044. [CrossRef]
56. Kohmoto, M.; Sutherland, B.; Tang, C. Critical wave functions and a Cantor-set spectrum of a one-dimensional quasicrystal model. *Phys. Rev. B* **1987**, *35*, 1020–1033. [CrossRef]
57. Siebesma, A.P.; Pietronero, L. Multifractal Properties of Wave Functions for One-Dimensional Systems with an Incommensurate Potential. *Europhys. Lett.* **1987**, *4*, 597. [CrossRef]
58. Hiramoto, H.; Kohmoto, M. Scaling analysis of quasiperiodic systems: Generalized Harper model. *Phys. Rev. B* **1989**, *40*, 8225–8234. [CrossRef]
59. Hiramoto, H.; Kohmoto, M. Electronic spectral and wavefunction properties of one-dimensional quasiperiodic systems: A scaling approach. *Int. J. Mod. Phys. B* **1992**, *6*, 281–320. [CrossRef]
60. Maciá, E. On the Nature of Electronic Wave Functions in One-Dimensional Self-Similar and Quasiperiodic Systems. *ISRN Condens. Matter Phys.* **2014**, *2014*, 165943. [CrossRef]
61. Wu, A.K. Fractal Spectrum of the Aubry-André Model. *arXiv* **2021**, arXiv:2109.07062.
62. Geisel, T.; Ketzmerick, R.; Petschel, G. New class of level statistics in quantum systems with unbounded diffusion. *Phys. Rev. Lett.* **1991**, *66*, 1651–1654. [CrossRef]
63. Harper, P.G. Single Band Motion of Conduction Electrons in a Uniform Magnetic Field. *Proc. Phys. Soc. A* **1955**, *68*, 874. [CrossRef]

64. Lahini, Y.; Pugatch, R.; Pozzi, F.; Sorel, M.; Morandotti, R.; Davidson, N.; Silberberg, Y. Observation of a Localization Transition in Quasiperiodic Photonic Lattices. *Phys. Rev. Lett.* **2009**, *103*, 013901. [CrossRef] [PubMed]
65. Roati, G.; D'Errico, C.; Fallani, L.; Fattori, M.; Fort, C.; Zaccanti, M.; Modugno, G.; Modugno, M.; Inguscio, M. Anderson localization of a non-interacting Bose–Einstein condensate. *Nature* **2008**, *453*, 895–898. [CrossRef] [PubMed]
66. Lüschen, H.P.; Scherg, S.; Kohlert, T.; Schreiber, M.; Bordia, P.; Li, X.; Das Sarma, S.; Bloch, I. Single-Particle Mobility Edge in a One-Dimensional Quasiperiodic Optical Lattice. *Phys. Rev. Lett.* **2018**, *120*, 160404. [CrossRef] [PubMed]
67. De Tomasi, G.; Khaymovich, I.M.; Pollmann, F.; Warzel, S. Rare thermal bubbles at the many-body localization transition from the Fock space point of view. *Phys. Rev. B* **2021**, *104*, 024202. [CrossRef]
68. Roy, N.; Sharma, A. Entanglement entropy and out-of-time-order correlator in the long-range Aubry–André–Harper model. *J. Phys. Condens. Matter* **2021**, *33*, 334001. [CrossRef] [PubMed]
69. Ahmed, A.; Roy, N.; Sharma, A. Dynamics of spectral correlations in the entanglement Hamiltonian of the Aubry-André-Harper model. *Phys. Rev. B* **2021**, *104*, 155137. [CrossRef]
70. Aditya, S.; Roy, N. Family-Vicsek dynamical scaling and Kardar-Parisi-Zhang-like superdiffusive growth of surface roughness in a driven one-dimensional quasiperiodic model. *Phys. Rev. B* **2024**, *109*, 035164. [CrossRef]
71. Richerme, P.; Gong, Z.X.; Lee, A.; Senko, C.; Smith, J.; Foss-Feig, M.; Michalakis, S.; Gorshkov, A.V.; Monroe, C. Non-local propagation of correlations in quantum systems with long-range interactions. *Nature* **2014**, *511*, 198–201. [CrossRef]
72. Colmenarez, L.; McClarty, P.A.; Haque, M.; Luitz, D.J. Statistics of correlation functions in the random Heisenberg chain. *SciPost Phys.* **2019**, *7*, 064. [CrossRef]
73. Lezama, T.L.M.; Lev, Y.B.; Santos, L.F. Temporal fluctuations of correlators in integrable and chaotic quantum systems. *SciPost Phys.* **2023**, *15*, 244. [CrossRef]
74. Colbois, J.; Alet, F.; Laflorencie, N. Interaction-Driven Instabilities in the Random-Field XXZ Chain. *arXiv* **2024**, arXiv:2403.09608.
75. Available online: www.hpc-rivr.si (accessed on 31 May 2024).
76. Available online: https://eurohpc-ju.europa.eu/ (accessed on 31 May 2024).
77. Available online: www.izum.si (accessed on 31 May 2024).